Available online at www.sciencedirect.com

jmr&t Journal of Materials Research and Technology

journal homepage: www.elsevier.com/locate/jmrt

Original Article

The effect of the ultrasound agitation and source of ceria particles on the morphology and structure of the Zn–Co–CeO_2 composite coatings

Marija Rićošić [a,b], *Asier Salicio-Paz* [c], *Eva García-Lecina* [c], *Piotr Zabinski* [d], *Ljiljana S. Živković* [e], *Jelena B. Bajat* [a,*]

[a] *University of Belgrade, Faculty of Technology and Metallurgy, Karnegijeva 4, 11000, Belgrade, Serbia*
[b] *University of East Sarajevo, Faculty of Technology Zvornik, Karakaj 34A, 75400, Zvornik, Republic of Srpska, Bosnia and Herzegovina*
[c] *CIDETEC Basque Research and Technology Alliance (BRTA), Donostia-San Sebastián, Spain*
[d] *AGH University of Science and Technology, Faculty of Non-Ferrous Metals, al. Mickiewicza 30, 30-059, Krakow, Poland*
[e] *University of Belgrade, Vinča Institute of Nuclear Science, Belgrade, Serbia*

ARTICLE INFO

Article history:
Received 17 January 2021
Accepted 23 May 2021
Available online 28 May 2021

Keywords:
Corrosion
Nanocomposite coatings
CeO_2 nanoparticles
Self-healing
Surface characterization
Ultrasound

ABSTRACT

The goal of this research was to develop and analyse novel Zn–Co–CeO_2 protective coatings on steel. Two different sources of ceria (CeO_2) particles were employed: commercial powder and synthesized stable colloidal dispersion-sol. The plating solution was agitated by ultrasounds (20 and 30 W cm^{-2}) or by magnetic stirrer (300 rpm) during electrodeposition. The CeO_2 particles used were characterized by different methods, namely scanning electron microscopy (SEM), transmission electron microscopy (TEM) and X-ray diffraction (XRD) to compare the morphology, crystallinity and particle size. The morphology of developed composite coatings was analysed by SEM, the preferred texture was calculated based on XRD results and corrosion behaviour was evaluated by electrochemical impedance spectroscopy (EIS) and polarization measurements. Utilizing ultrasounds during electrodeposition resulted in advanced properties of the nanocomposite coatings compared to magnetic stirring. The particle content in the coatings increased to ~5 wt% when ultrasounds were applied and ceria sol used as a source of particles. Presence of ceria in composite coatings offered favourable action in corrosion behaviour increasing barrier properties of composite coatings, thereby providing a prolonged lifetime of Zn–Co alloy coatings. The benefit was more pronounced in the case of ceria sol, and deposition at 20 W cm^{-2}, when values of impedance modulus at low frequencies reached four times higher values after 4 days exposure to 3 wt% NaCl solution than for coatings deposited with magnetic stirring for both ceria source. The lowest value of corrosion current density (2.15 μA cm^{-2}) was determined for Zn–Co–CeO_2 (CeO_2 sol) composite coatings deposited under 20 W cm^{-2} US power.

* Corresponding author.
E-mail address: jela@tmf.bg.ac.rs (J.B. Bajat).
https://doi.org/10.1016/j.jmrt.2021.05.064

1. Introduction

Coatings are widely used in various industrial areas for improving a wide range of surface properties (i.e. hardness, wear, corrosion resistance). Steel protection is mostly accomplished by Zn and Zn-based coatings depending on the final application. On one hand, large steel parts are mainly protected by galvanizing, whereas small steel pieces are commonly protected by Zn alloy coatings produced by electrodeposition. Recently, a lot of attention has been paid to the co-deposition of Zn with various micro/nanoparticles, in order to tune the properties of metal matrix composite layers for a variety of applications [1–6]. For instance, Zn–TiO_2 [7], Zn–SiO_2 [3], Zn–ZrO_2 [8] or Zn–Ni–Al_2O_3 [9] are reported as materials with enhanced hardness, wear and corrosion resistance in comparison with the bare metallic coating. Moreover, the incorporation of ceria (CeO_2) particles into the metal matrix [1,4,5], as corrosion inhibitor, results in an improved corrosion resistance due to its ability to block corrosion active sites and its self-repairing character. The ceria particles actually might be a complex oxide containing both Ce^{3+} and Ce^{4+} [10–13]. Among different available coating deposition routes, like PVD, CVD, plasma spaying, high velocity oxygen fuel flame spraying, electrodeposition showed several advantages including control of coating thickness, versatility, high current efficiency and reasonable costs together with the ability to deposit coatings on complex shapes [14]. The main drawback in the incorporation of micro/nano particles via electro-co-deposition processes is the low dispersion stability of particles in plating baths due to their high ionic strength [9]. Consequently, the agglomeration of particles in such media is difficult to avoid. The most common strategies carried out for minimizing particle agglomeration are: magnetic and mechanical stirring [4], wet ball milling [15], both prior and/or during electrodeposition. Lately, ultrasonic agitation [16,17] has emerged as a promising method for promoting the electrodeposition of nanocomposite coatings. The ultrasounds applied during electrodeposition can enhance the mass transfer, ensuring higher current efficiency [18,19], cleaning the cathode and mitigating the porosity development caused by hydrogen evolution. The use of ultrasounds allows better dispersity of the second phase in the solution promoting de-agglomeration, especially when very small particles are used. Furthermore, the use of ultrasounds affects the quality and properties of the produced coatings as they can facilitate the incorporation of the particles in the composite coatings, change the microstructure and reduce grain size. Contrary to Zn-composite systems, very few works have been published on Zn-alloy composites. Among Zn alloys, Zn–Ni composite coatings [5,6,9] were mostly analysed but there are only few reports on protective Zn–Co composite coatings [20,21]. To the best of our knowledge, there are no publications on Zn–Co–CeO_2 nanocomposite coatings available in the literature. Zn–Co coatings with low Co content exhibit good corrosion behaviour, qualifying them as good alternative for enhancing the durability of zinc coatings [21–23].

In this work, in order to analyse corrosion behaviour of zinc alloy composites, protective Zn–Co coatings containing ceria nanoparticles were electrodeposited on steel substrates. Ceria, a well-known corrosion inhibitor [10], was co-deposited from 2 different sources: laboratory synthesized ceria sol, and commercial ceria powder. According to literature [2–5,7–9], metal oxide particles are mostly introduced in the plating bath as powder nanoparticles, which are very prone to agglomeration. Thus, the idea behind this work was to use an in-house synthesized stable dispersion of ceria nanoparticles (sol) as a source of ceria. The influence of the plating solution agitation was studied in parallel by applying ultrasound (US), generated by US horn, or by use of magnetic stirrer. Different US power intensities were evaluated. Thus, a combination of ceria-sol along with ultrasonic stirring was investigated for minimizing the undesirable phenomenon of particle agglomeration in composite plating baths.

2. Experimental

2.1. Characterization of the particles

Two ceria sources were used-ceria in the form of powder and colloidal dispersion of ceria. The commercial ceria powder used was produced by Merck.

Stable aqueous colloidal dispersion (sol) was prepared by forced hydrolysis of precursor cerium (IV)-nitrate ($Ce(NO_3)_4$) (1 N aq. solution) (Alfa Aesar). The ceria sol was prepared following the procedure described by Stevanović et al. [10]. The sol was dialyzed against distilled water up to $pH = 3$. Solid content was 2 g dm^{-3}. To obtain information about the morphology, size and shape of the particles, the samples were analysed by scanning electron microscopy (SEM, Ultra Plus, Carl-Zeiss) and transmission electron microscopy (TEM, Tecnai TF 20 X-TWIN operated at 200 kV and with magnification 1025–900 k respectively). The X-ray diffraction (XRD) patterns were recorded by Rigaku Mini Flex diffraction instrument using the Cu 1 kW radiation. The average crystallite sizes were calculated from the original diffraction data according to the Scherrer equation [8]. The solid phase from homemade ceria sol and ceria powder samples were placed directly on the XRD measurements holder. The scan range used was 10–100°, with 0.01° step. The chemical composition and oxidation state of synthesized ceria sol were analysed by X-ray photoelectron spectroscopy (XPS). The XPS analyses were carried out in a PHI Versa ProbeII Scanning XPS system using monochromatic Al Kα (1486.6 eV) X-rays focused to a 100 μm spot and scanned over the area of 400 × 400 μm. The photoelectron take-off angle was 45° and the pass energy in the analyzer was set to 117.50 eV (0.5 eV step) for survey scans and 46.95 eV (0.1 eV step) to obtain high energy resolution spectra for the C 1s, O 1s, N 1s and Re 4f regions. Dual beam charge compensation with 7 eV Ar^+ ions and 1 eV electrons were used to maintain a constant sample surface potential

Table 1 – Process parameters and plating bath composition.

Plating bath composition	Plating parameters
$ZnCl_2$: 0.1 mol dm^{-3} H_3BO_3: 0.8 mol dm^{-3} KCl: 3 mol dm^{-3} $CoCl_2 \cdot 6H_2O$: 0.03 mol dm^{-3} CeO_2 (sol and powder): 0.0116 mol/dm^{-3}	Current density: 2 A dm^{-2} Temperature: 24 ± 2 °C Deposition time = 30 min Stirring: magnetic stirring 300 rpm or ultrasound stirring produced by ultrasonic horn, placed between cathode and anode, avoiding shielding (Hielscher Ultrasonics GmbH) with a sonotrode S14 (14 mm tip diameter)) (20 and 30 W cm^{-2}) Cathode: low-carbon steel (AISI-1010) flat panels (plating area 1 cm × 2 cm) Anode: two anodes of pure zinc (1 cm × 2 cm) pH = 3

regardless of the sample conductivity. All XPS spectra were charge referenced to the unfunctionalized, saturated carbon (C–C) C 1s peak at 285.0 eV. The operating pressure in the analytical chamber was less than 3×10^{-7} mbar. Deconvolution of spectra was carried out using PHI MultiPak software (v.9.9.0.8). Spectrum background was subtracted using the Shirley method.

2.2. *Deposition and characterization of the Zn–Co–CeO_2 coatings*

The deposition of the Zn–Co–CeO_2 composite coatings was carried out galvanostatically; composition and plating parameters are summarized in Table 1.

The deposition was carried out in a double-jacket glass cell (0.200 dm^{-3}) with precise electrolyte temperature control. The schematic presentation of sonoelectrochemically co-deposition of Zn–Co with ceria particles is shown in Fig. 1. When the power source was turned on, the electric field was

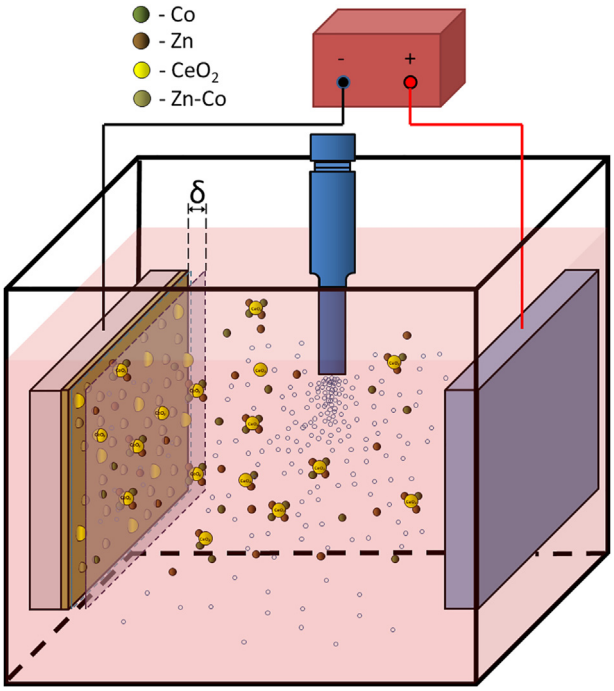

Fig. 1 – Schematic presentation of the co-deposition process of Zn–Co–CeO_2 composite coatings in the presence of US horn; δ-electric double layer.

established between anode and cathode. Metal ions (Zn^{2+} and Co^{2+}), and positively charged ceria particles, were transported towards cathode surface by electric force and stirring. The ultrasonic stirring of the plating solution enhances the transport of particles towards the cathode, most significantly in comparison to magnetically stirring. The Zn^{2+} and Co^{2+} ions are smaller compared to the ceria particles and thus easily adsorbed and reduced on the cathode surface. Ceria particles were first weakly adsorbed onto the cathode and then entrapped by the growing Zn–Co metal matrix [24]. The commercial CeO_2 powder and synthesized CeO_2 sol were used as the source of ceria particles in the different plating solutions. When sol was used, all bath components were dissolved into the prepared ceria sol solution. On the other hand, when ceria powder was used as source of the particles, all components were dissolved in double distilled water and pH was adjusted to 3. Before deposition, the plating solutions were agitated by magnetic stirring for 24 h. The morphology and composition of the obtained coatings were analysed by Ultra Plus, Carl-Zeiss scanning electron microscopy coupled with an Ametek® EDAX, APOLLO X energy dispersive spectroscopy probe. Crystallinity of the coatings was studied by D8, Bruker X-ray diffraction using the CuKα radiation in the Bragg–Brentano geometry. Corrosion behaviour of deposited composite coatings in 3 wt% NaCl was examined by electrochemical impedance spectroscopy, by Reference 600 potentiostat/galvanostat/ZRA Gamry Instruments. For these measurements, deposition time was calculated according to Faradays' law in order to obtain 10 μm thick coatings. The corrosion tests were performed at room temperature (RT) in three-electrode corrosion cell. The composite coating was working electrode (1.0 cm^2 area), a platinum grid was used as counter electrode and saturated calomel electrode was the reference electrode. Electrochemical impedance tests were performed at open-circuit potential, 100 kHz–0.01 Hz frequency range, with 10 mV amplitude and 7 points/decade. The polarization measurements were performed after establishing stable open circuit potential (~60 min), with the scan rate of 0.25 mV s^{-1}.

3. Results and discussion

3.1. *Particles characterization*

The ceria particles in sol (aqueous colloidal dispersion) were well dispersed and stable showing high positive surface

charge (Z-potential 51.2 ± 0.5 mV), as reported in previous research [10]. The sol particles exhibited monomodal and narrow size distribution (PSD) in approximate range of 30–110 nm, with average size for hydrodynamic diameter of $Z_{aver.}$ 60 nm [10]. The diffraction patterns for the commercial CeO_2 powder and solid phase of synthesized ceria sol were compared in the whole compositional range and results are shown in Fig. 2. According to XRD diagrams, both analysed samples are single-phased CeO_2 since no additional peaks relative to other phases were present. The peaks shown in XRD spectra in Fig. 2 were indexed as cubic phase typical for the fluorite ceria structure (space group: Fm3m, JCPDS 34-0394). Additionally, both examined samples displayed the peaks that match (111), (200), (220), (311), (222), (400), (331), (420), (422) and (333) planes, confirming the cubic fluorite structure of CeO_2 in the standard data. It is clearly seen that reflection peaks for the homemade particles were broader and of weaker intensities compared to commercial ceria particles, suggesting smaller crystallite size and lower

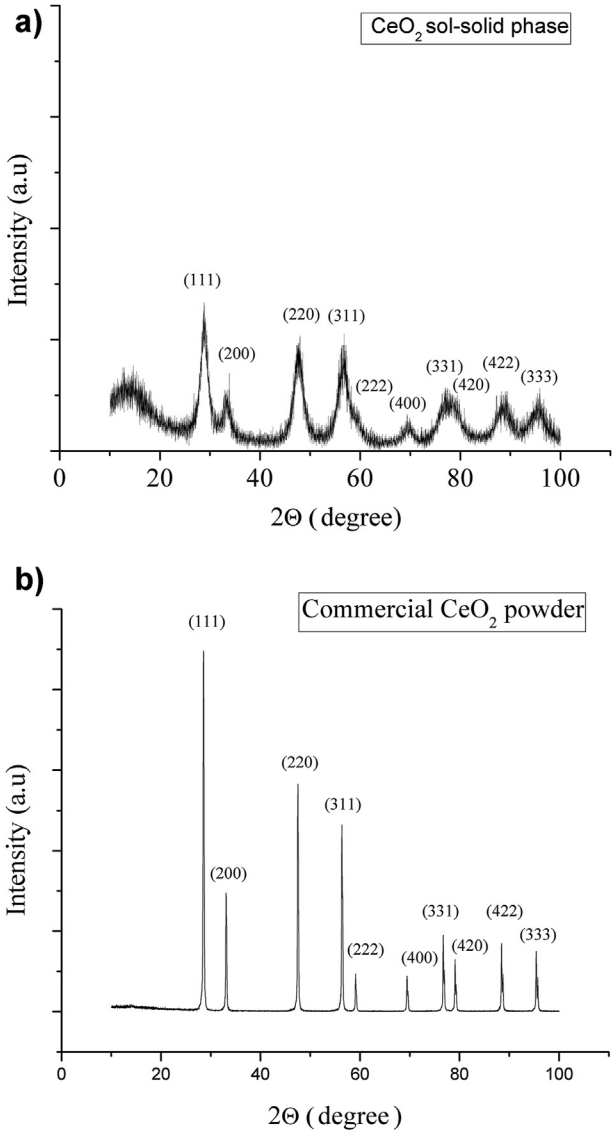

Fig. 2 – XRD pattern of a) solid phase of synthesized ceria sol b) commercial ceria powder.

crystallinity [25,26]. The average crystallite size, calculated according to the Scherrer equation [8], of the synthesized ceria (solid phase) sample was 4 nm whereas the commercial ceria powder showed sizes of 35 nm, more than 8 times bigger than the former. The morphology of the ceria powder is shown in Fig. 3. The small particles of different sizes, in a nanometre range, could be clearly seen in Fig. 3a, supporting XRD results. Some of the particles are packed in small ceria clusters/agglomerates, observed as white forms in Fig. 3a. The SEM micrograph of ceria powder at different spots (Fig. 3b) reveals the presence of larger agglomerates, as well. Agglomeration is a well-known phenomenon occurring in nanosized powders, due to the tendency of very fine particles to minimize the surface energy by clustering [27]. The size and morphology of the ceria particles in sol were examined using TEM. Fig. 4a shows the bright-field TEM image of the synthesized ceria sample. Notably, numerous clear particle boundaries could be observed within individual particle aggregate showing size up to 30 nm, demonstrating that each one is actually composed of smaller units. This is in line with particle size distribution (PSD) analysis, which measured hydrodynamic size of particles, thus the dimensions were somewhat bigger [10]. Hence, ceria particles also showed a strong agglomeration tendency during dehydration. TEM study (Fig. 4b) confirms the presence of the very small crystallites in the size range of 2–5 nm, as building units of bigger particles. These observations are in good agreement with crystallite size calculated based on XRD results. The crystalline structure was evaluated by selected area electron diffraction (SAED) analysis (Fig. 4c). The SEAD pattern of the synthesized ceria particles revealed a succession of bright diffraction rings pointing to its polycrystalline structure. The broadening of the diffraction rings indicates very small particles highlighting the nanocrystalline nature of the particles [28,29]. All the diffraction rings can be indexed to the cubic CeO_2 phase, confirming the assumption from the XRD data. Determined interplanar spacing, ($d_{(hkl)}$) from the SAED pattern was in good agreement with gained XRD results as well as the standard data, as shown in Table 2. In order to study also the valence state of cerium in the synthesized ceria sol particles, the XPS measurements were performed. As already mentioned, both Ce^{3+} and Ce^{4+} oxidation state are present in ceria particles [10–13,30–35], and the amount of Ce^{3+} increases with decreasing size of particles [12,13]. It was important to detect and determine the presence and amount of the Ce^{3+} ions in ceria particles because they greatly affect the properties of the material. Namely, the increase in Ce^{3+} concentration causes increase in oxygen vacancies concentration and unsaturated bonds, which are responsible for various applications of ceria, i.e. fuel cells, advanced catalytic, photocatalytic, medical [11–13,33–37]. Besides, the Ce^{3+}ions in ceria particles play an important role in advanced corrosion protection of ceria doped coatings and imparts self-healing effect [35–37]. The Ce3d and O 1s spectrum of synthesized ceria sol obtained by XPS spectra are presented in Fig. 5. The Ce3d spectrum confirms the presence of both Ce^{4+} and Ce^{3+} state, where spin-orbits labelled as υ_o, υ', u' at 881.5, 884.4 and 902.5 eV correspond to Ce^{3+}, while υ, υ'', υ''', u, u'', u''' at 882.6, 888.9, 898.8, 900.8, 907.8, 917.2 eV are attributed to Ce^{4+}. Following the calculation procedure

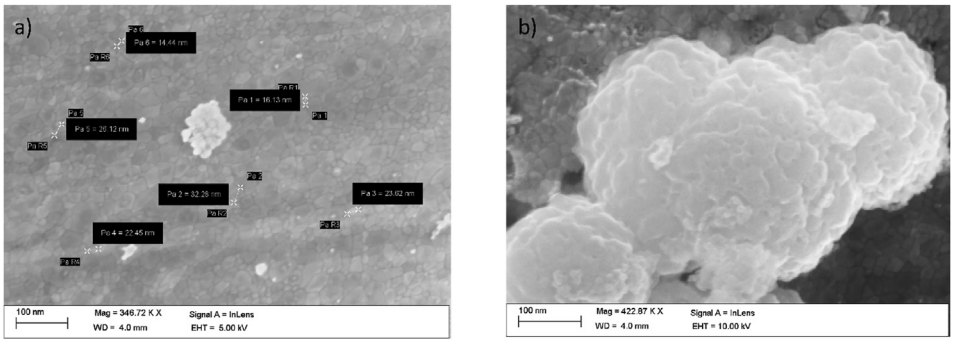

Fig. 3 – Micrographs of CeO_2 powder showing: (a) smaller and (b) bigger ceria clusters/agglomerates.

presented in [33], the significant amount of Ce^{3+} in ceria sol nanoparticles was determined (27%), leading to Ce^{3+}/Ce^{4+} ratio of 0.37. The O 1s spectrum was resolved into tree peaks. The peaks at high binding energy (531.3 and 533.5 eV) correspond to organic C–O and C=O bonds and the peak at low binding energy (529.1 eV) corresponds to O–Ce bond [38].

3.2. *Characterization of Zn–Co–CeO_2 nanocomposite coatings*

3.2.1. *Coatings morphology*

The morphology and cross section of composite coatings, electrodeposited galvanostatically from different CeO_2 particles sources and different type of stirring, are shown in Fig. 6. The influence of the agitation type on the appearance and structure of composite coatings is clear. Electrodeposition with magnetic stirring results in heterogeneous and irregular structure of the composite coatings, resulting in the formation of different patterns, for both types of ceria particles sources as can be seen from Fig. 6. When ceria powder is used, large agglomerates are visible in top-view of the coatings, thus indicating that magnetic stirring was not sufficiently powerful for de-agglomeration purposes (insert in Fig. 6a). The protrusion clusters visible on the top of the coating are made of many small needle-like crystals. The cross section (Fig. 6b) images reveal the irregular growth of the coating and its highly porous nature. When ceria sol was used, more homogeneous microstructure was observed derived from the absence of large agglomerates due to uniformly distributed particles, although it remains porous as can be noticed in top surface view (Fig. 6g). The cross section analysis (Fig. 6h) indicates the coarse growth and low compactness of the obtained coating. The 3D irregular growth of the coatings obtained by magnetic stirring (Fig. 6b and h) is related to the non-uniform distribution of electric field. When any protuberance is formed on the growing surface, the ions are preferentially reduced on such bulges due to "tip discharge effect" [24,38] resulting in larger nodules during advancement of the deposition time. When sonoelectrodeposition (20 W cm^{-2}) was applied, the enhancement in quality and morphology of

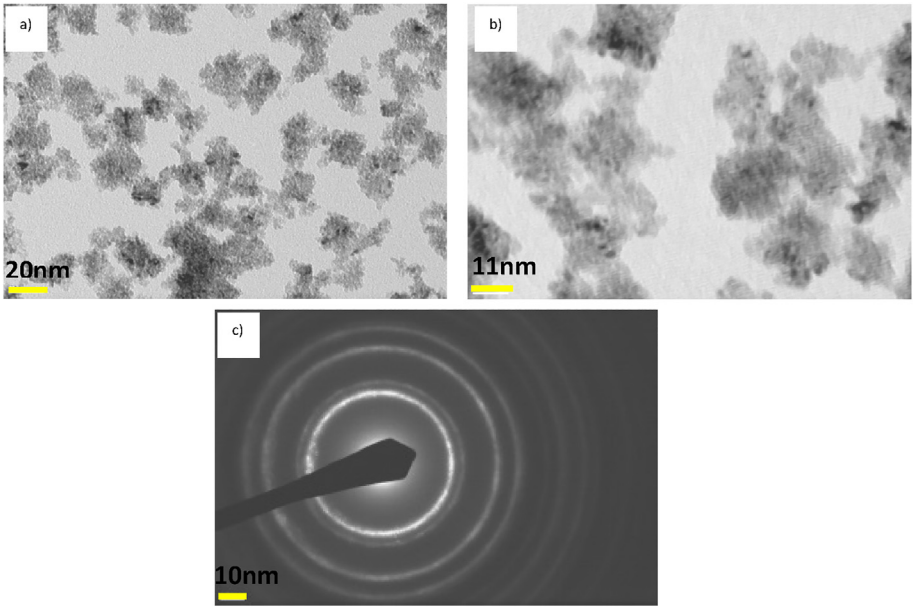

Fig. 4 – TEM image of the prepared ceria nanoparticles (CeO_2 sol) at different magnification: a) and b), c) SAED pattern.

Table 2 – Determined interplanar spacing ($d_{(hkl)}$ (nm)), obtained from SAED pattern (shown in Fig. 4c) and XRD results of ceria particles in sol.

SAED results		XRD results		Standard data (JCPDS 34-0394)		
Diffraction ring	$d_{(hkl)}$ (nm)	2θ(°)	$d_{(hkl)}$ (nm)	2θ(°)	$d_{(hkl)}$ (nm)	h k l
R_1	0.3352	29.02	0.3074	28.67	0.3114	(111)
R_2	0.2977	33.67	0.2659	33.22	0.2695	(200)
R_3	0.2094	47.74	0.1903	47.69	0.1905	(220)
R_4	0.1791	56.18	0.1635	56.59	0.1625	(311)

both coating systems was visible (Fig. 6c and i). The surface was flat, uniform and compact. No voids, cracks or other defects were noticeable. The cross sectional view confirmed dense, fully adhered coatings, and uniformly deposited throughout the substrate. When the ultrasound field is established in the plating electrolyte, various cavitation phenomena could be induced (i.e. micro-jetting, acoustic streaming, shock waves, etc.), enhancing the mass transfer during the electrodeposition process [18]. As a result, the surface of the cathode is cleaned by hydrogen bubbles. Thus, the obtained coating is denser and smoothly finished. The ultrasound applied enables the de-agglomeration of ceria powder particles and also depresses (re-)aggregation aided by the existence of micro-turbulence in solution. Accordingly, the presence of high speed bubbles is capable of breaking strong van der Waals forces existing among particles in agglomerates, as proven by absence of large agglomerates when ceria powder is used (Fig. 6c). Therefore, the US promotes good dispersion of particles and maintains the overall homogeneity of the plating solution. The ultrasound affects also the grain size of the produced nanocomposite coatings as can be seen from the FESEM images. The grain size is reduced due to the influence of above mentioned cavitation related effects. The applied ultrasounds produce vesicles which hit the surface, modifying the cathode surface, making it rougher and increasing the number of active sites on the cathode and, as a consequence, the nucleation is faster and the grain size of the deposits smaller (Fig. 6c and i). In addition, when using ultrasounds during electrodeposition both, the metal ions and ceria in the solution are transported faster towards the electrode surface where nanometric particles are easily and uniformly adsorbed onto the growing crystals, like schematically presented in Fig. 1, hindering their further growth and resulting in smaller grain size. Although the use of ultrasound improved the structure of the Ce-containing coatings compared to magnetic stirring results, a beneficial influence of the ceria sol addition was also visible. The Zn–Co–CeO_2 (CeO_2 sol) coating (Fig. 6j) was more compact, and void-less compared to Zn–Co–CeO_2 (CeO_2 powder) (Fig. 6d). However, the increase in ultrasound power from 20 to 30 W cm^2 resulted in the increase in the grain size and formation of a rougher microstructure regardless the source of ceria particles (Fig. 6e and k). However, the decrease in homogeneity and compactness was more pronounced when ceria sol was used (Fig. 6k,1 compared to Fig. 6e,f). This effect could be due to highly forced convection in plating solution, resulting in formation of increased number of "bubbles" in solution which violently strike the growing coating [7,16,23]. The composition of the obtained composite coatings was determined by EDS and the results are shown in Table 3. For ceria-sol based composite coatings the higher the ultrasound power the higher the content of Ce in the coatings (i.e. CeO_2 particles). Conversely, when composite coatings were deposited from a solution containing ceria powder as a source of Ce, the content of Ce was lower for higher ultrasound power. Two phenomena

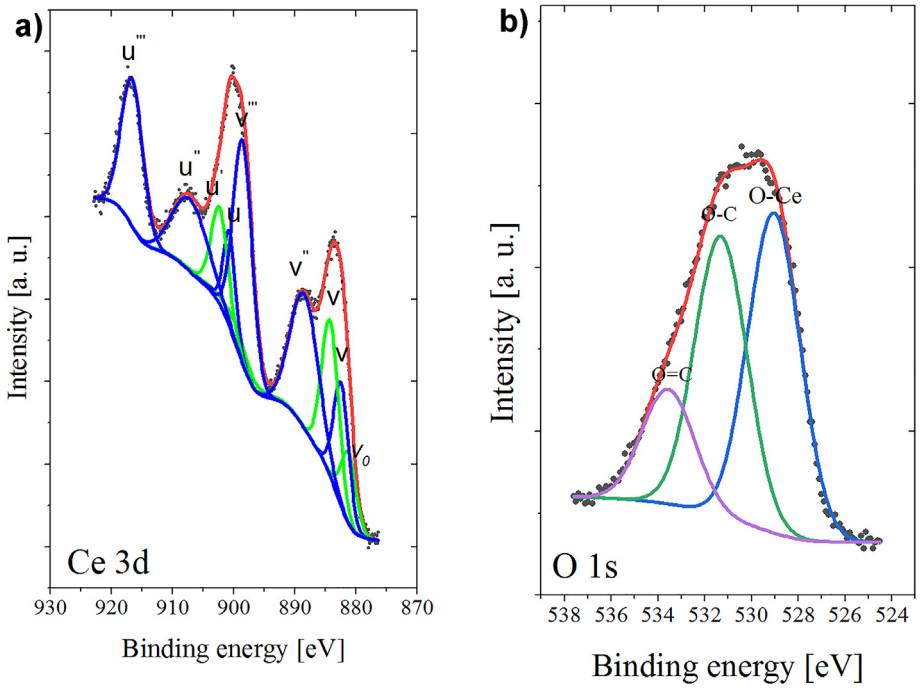

Fig. 5 – XPS spectrum of ceria particles, a) Ce3d spectrum, b) O 1s spectrum.

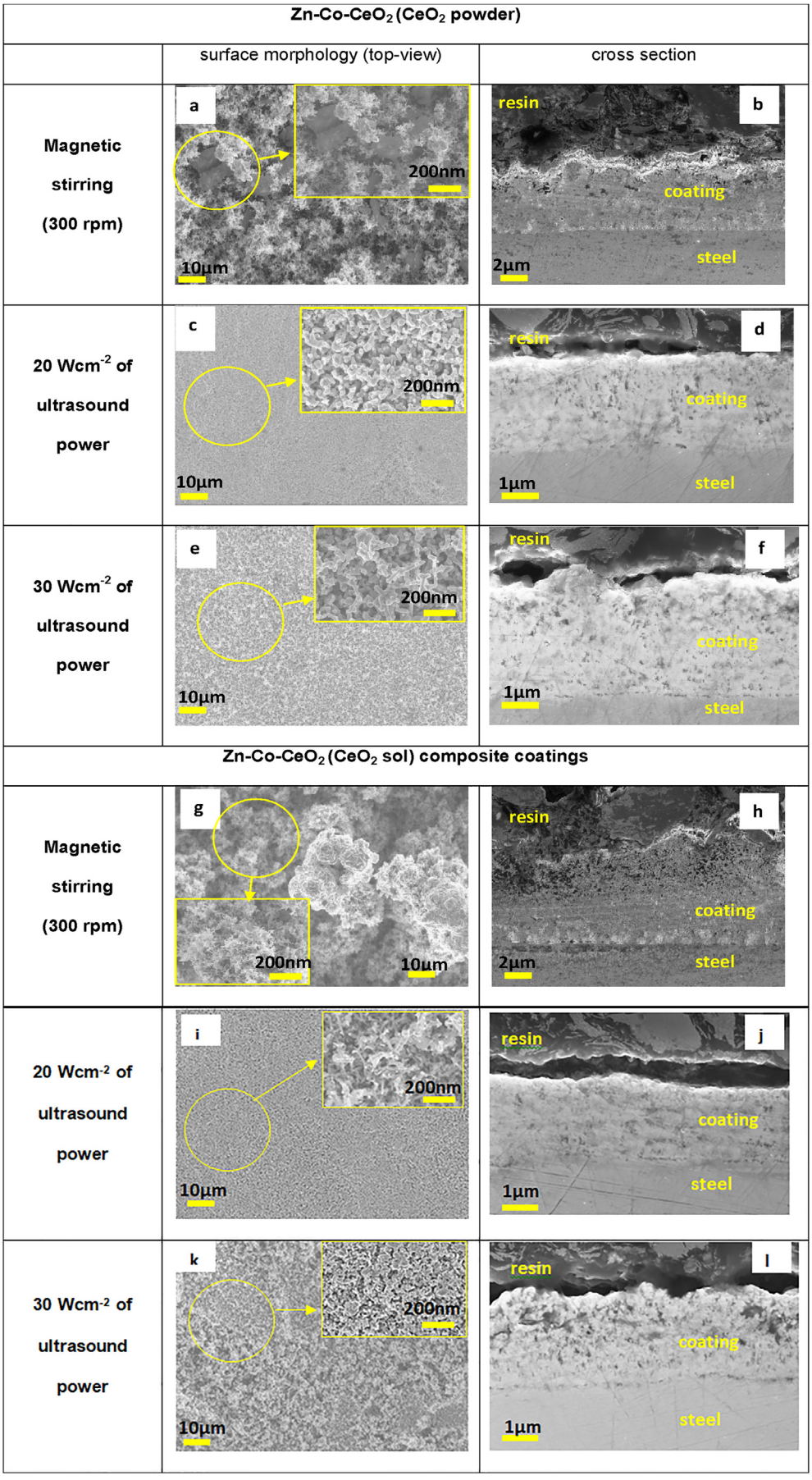

Fig. 6 – FESEM micrographs of the Zn–Co–CeO_2 (CeO_2 powder) and Zn–Co–CeO_2 (CeO_2 sol): a) magnetic stirring, b) 20 W cm^{-2}, and c) 30 W cm^{-2} of US power.

Table 3 – The chemical composition of Zn–Co–CeO_2 composite coatings (wt%).

Element/Compound	Zn–Co–CeO_2 (CeO_2 sol)			Zn–Co–CeO_2 (CeO_2 powder)		
	Magnetic stirring	20 W cm^{-2}	30 W cm^{-2}	Magnetic stirring	20 W cm^{-2}	30 W cm^{-2}
Co	1.58	3.27	4.27	1.88	2.77	2.42
Ce	2.25	3.06	4.97	1.00	2.05	0.95

could be supposed during deposition related to larger ceria particle size.

Namely, the too strong agitation caused collisions between the particles and the growing layer (Fig. 7a), so the great number of particle was bounced off the surface (Fig. 7b). Besides, the applied high ultrasound power can easily remove the weakly adsorbed larger particles (Fig. 7c) from the cathode surface [39] before they become incorporated into a growing layer drawing them back into the solution (Fig. 7d). Table 3 therefore confirms that small ceria sol particles were more easily incorporated into the growing coatings, resulting in greater cerium content. Both sol and US were also beneficial for Co incorporation.

On the basis of the results presented in Table 3, it could be concluded that the deposition of Zn–Co–CeO_2 composite coatings was of anomalous type [14,40]. Namely, the Co content in the coatings is ranging from 1.5 to 4.3 wt%, which is well below the amount of 23.1 wt%, that corresponds to a composition reference line (CRL). The CRL represents the ratio of Co to the overall amount of Co and Zn in the plating solution [40]. According to Brenner [40] such behaviour indicates the preferential deposition of less noble element, Zn.

3.2.2. *XRD characterization*

XRD diffractograms of the Zn–Co–CeO_2 composite coatings are shown in Fig. 8. All obtained diffractograms consisted of peaks corresponding to η-Zn phase, due to low content of Co which is completely dissolved in Zn lattice, in accordance with other reports [41–44]. The ceria related peaks were not detected by XRD method, as expected, due to the small amount of the incorporated particles (for both ceria sources used) which lies below 5 wt% resulting in the absence of the corresponding diffraction peaks as reported elsewhere [45–47]. Nevertheless, the presence of cerium was confirmed by EDS analysis, as shown in Table 3. However, the incorporation of ceria particles in Zn–Co alloy caused perturbation in crystal lattice and, as a consequence, the shift in the peaks 2θ values was noticed. This shift was more pronounced for deposits with greater amount of incorporated ceria (20 and 30 W cm^{-2} US power, CeO_2 sol). The (002) peak in XRD pattern of Zn–Co alloy deposited under magnetic stirring was positioned at $2\theta = 36.237°$ [23], while the same peak is present at $2\theta = 36.206°$ and $2\theta = 36.194°$ when ceria was incorporated as powder and sol, respectively. The shift to lower 2θ values was more pronounced with higher amount of incorporated ceria. When 30 W cm^{-2} US power was applied, the (002) peak in XRD pattern for Zn-Co [23] appeared at $2\theta = 36.193°$, however, for nanocomposite containing 4.97 wt% of CeO_2 (30 W cm^{-2} US power, CeO_2 sol), the peak was shifted towards lower angle values reaching $2\theta = 36.152°$. The same shift direction was noticed for (101) plane, from 43.165° for Zn-Co [23] to 43.084° for composite coating, and (112) plane displacement from 82.231° to 82.227°. Such results confirm that presented shift is a consequence of incorporated particles, and more pronounced when amount of particles is higher.

In order to examine the crystal preferential growth of the composite coatings, the relative texture coefficient (RTC) was calculated according to Berube method, described in detail in [48] and the results are presented in Fig. 9. Seven reflections were analysed in this work, and if the preferred orientation is present the RTC coefficient is higher than 14.3% (value marked by horizontal line in Fig. 9); when RTC value is lower than 14.3% the crystals are randomly orientated. The incorporation of the particles into the deposit has a large influence on the preferred orientation of the coatings [8,42,49]. The magnetic stirring of plating solution during deposition of Zn–Co alloy resulted in random orientation of crystals in Zn–Co alloy, as shown in [23]. When ceria particles in the form of powder were incorporated (Fig. 9a), the texture changed from random to prismatic (100) (RTC = 31%) along with pyramidal (101) planes with lower RTC value (19.7%). Applied ultrasound (20 W cm^{-2}) during electrodeposition of Zn–Co alloy resulted in increase of RTC value of (112) plane, but with significant contribution of (101), (100) and (002) planes [23]. When ceria

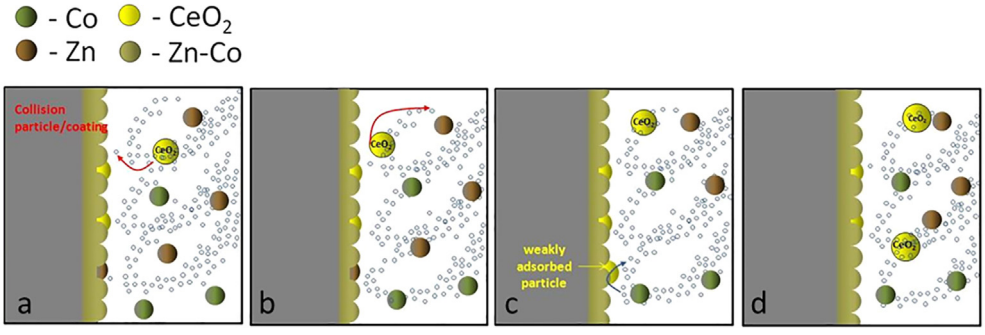

Fig. 7 – Schematically presentation of negative influence of too powerful agitation on powder particles.

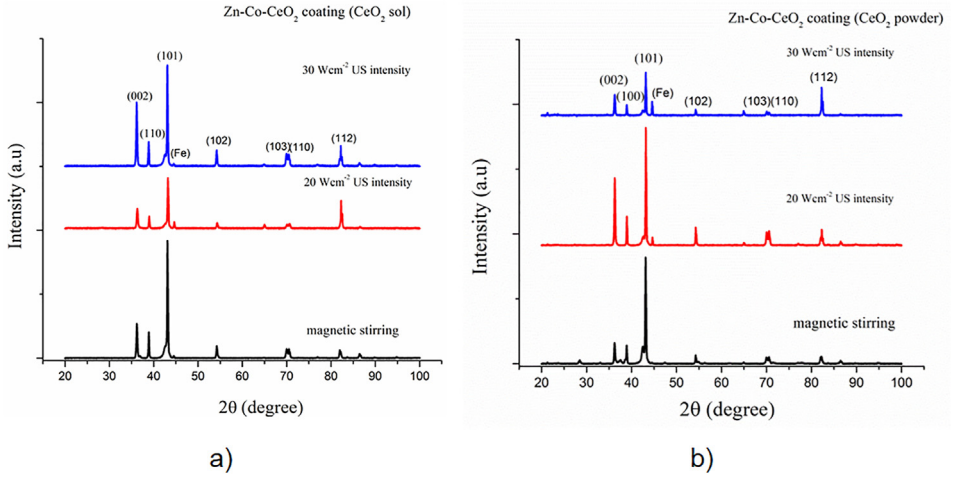

Fig. 8 – XRD diffractograms of the a) Zn–Co–CeO_2(CeO_2 sol) and b) Zn–Co–CeO_2 (CeO_2 powder) composite coatings obtained by different agitation methods: magnetic stirring, 20 W cm^{-2} and 30 W cm^{-2} ultrasound intensity.

particles originating from ceria sol were incorporated in Zn–Co alloy under the same plating conditions, 42.6% of crystal were orientated parallel to (112) plane (Fig. 9b). During the formation of nanocomposite coatings, the pyramidal deposit texture promotes a less ordered growth and those deficiencies promote keeping the particles on the electrode surface for longer times and, subsequently, facilitating their incorporation in the growing metal layer. When ceria commercial powder was used as a source of the second phase in the plating solution, pyramidal preferential orientation was not sufficient to enhance the incorporation of ceria particles in deposit, most likely due to ease of removing the ceria agglomerates from the electrode surface by applied ultrasound intensity. Based on the calculation of the crystal size (Scherrer equation [8]), the nanocrystalline size for all composite coatings was confirmed. The incorporation of ceria particles into Zn–Co matrix caused the small change in grains size. Namely, the crystallite size of Zn–Co matrix deposited under magnetic stirring was 31 nm [23], and when ceria was incorporated as ceria powder and ceria sol, the calculated grain size was 28 nm and 26 nm, respectively. When 20 W cm^{-2} ultrasound power was applied the matrix grain size [23] was considerably decreased to 22 nm and similar result was obtained for composite coatings: 21 nm Zn–Co–CeO_2 (CeO_2 powder) and 20 nm Zn–Co–CeO_2 (CeO_2 sol). The increase in ultrasound power (30 W cm^{-2}) resulted in Zn–Co deposits with the 39 nm grains [23] and when particles were incorporated as powder and sol, the grains were 29 nm and 25 nm, respectively.

3.2.3. *Corrosion resistance evaluation*

The corrosion resistance of the Zn–Co–CeO_2 nanocomposite coatings was evaluated using electrochemical impedance spectroscopy (EIS) and potentiodynamic polarization measurements in 3 wt% NaCl solution. The EIS was followed during 7 days (168 h) for all samples except for Zn–Co–CeO_2 (CeO_2 powder) deposited under magnetic stirring, since the appearance of red rust was visible on this sample already after 4 days, suggesting degradation of the coating and corrosion of the steel substrate. Such a fast failure was due to the rapid ingress of corrosion agent through a porous structure of this sample (Fig. 6a,b). The Nyquist plots shown in Fig. 10 reveal two depressed semi-circuits, indicating the deviation of the ideal dielectric behaviour. The nanocomposite coatings deposited with magnetic stirring showed the impedance arc depression, suggesting progress of corrosion and poor protective ability of these coatings, which could be expected based on their porosity and heterogeneous morphology, as shown by FESEM (Fig. 6a,d). The impedance of sonoelectrodeposited nanocomposite coatings increases with immersion time, indicating their good corrosion resistance. All

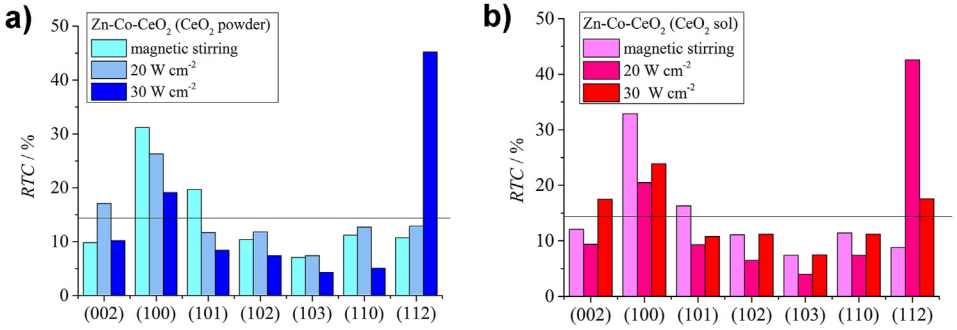

Fig. 9 – Relative texture coefficient of a) Zn–Co–CeO_2 (CeO_2 powder) and b) Zn–Co–CeO_2 (CeO_2 sol), obtained by different types of agitation.

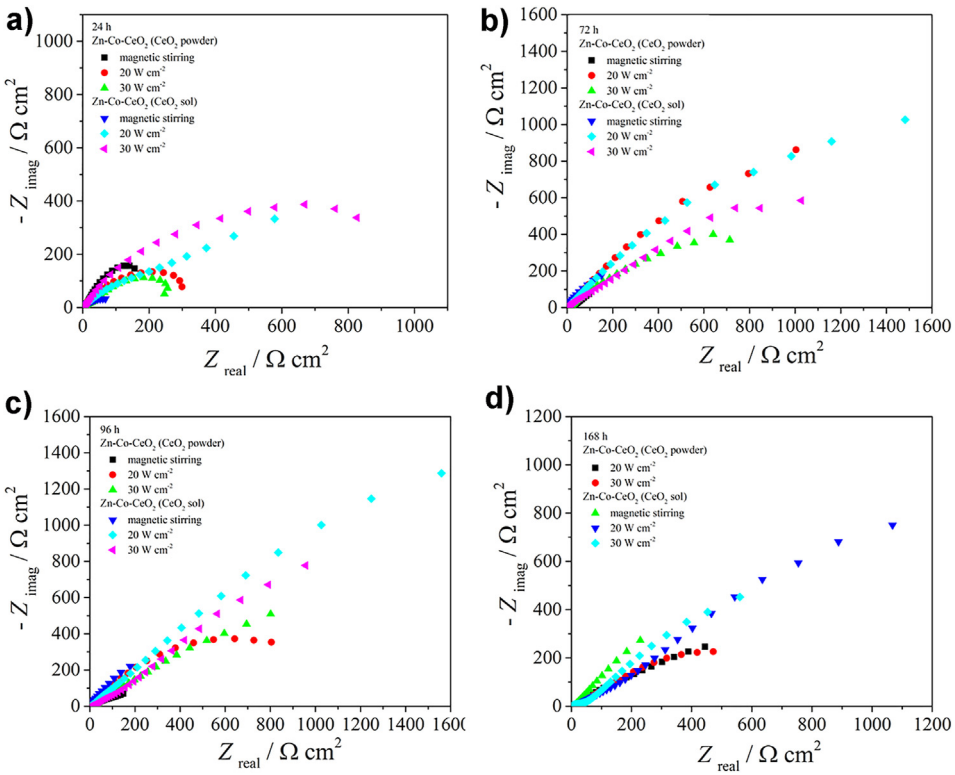

Fig. 10 – Nyquist plots for a) 24 h; b) 72 h; c) 96 h; d) 168 h exposure of Zn–Co–CeO_2 (CeO_2 powder) and Zn–Co–CeO_2 (CeO_2 sol) coatings to 3 wt% NaCl solution.

examined ceria-doped samples showed up to five times higher impedance as compared to pure Zn–Co alloy coatings deposited at same conditions [23]. The values of impedance modulus at low frequencies can be ascribed to processes on the steel/coating interface, such as the formation of a film of corrosion products, which may slow down the corrosion by partially blocking the diffusion of corrosion agents to the interface [35,50–52]. They could be used as effective tool for determining the corrosion resistance of the system. The values of impedance modulus at 10 mHz (Z_{mod} = 10 mHz) are shown in Fig. 11. As can be seen, all coatings showed slight decrease in Z_{mod} = 10 mHz value during first 24 h in NaCl solution, except of Zn–Co–CeO_2 (CeO_2 sol) under US power of 30 W cm^{-2}. The smallest Z_{mod} = 10 mHz values were obtained for the Zn–Co–CeO_2 composite coatings deposited under magnetic stirring of plating solution, regardless of the source of ceria particles, throughout all immersion period. Such behaviour could be expected based on the poor compactness of these deposits, as shown by FESEM results. Yet, the Zn–Co–CeO_2 (CeO_2 sol) system lasted 3 more days in corrosion media without red rust formation on the surface as compared to Zn–Co–CeO_2 (CeO_2 powder). The prolonged immersion life of this coating resulted from the higher amount of smaller and more uniformly distributed CeO_2 particles (from ceria sol) in coatings which are able to reduce the diffusion paths for corrosion agents due to blockage effect. However, the corrosion rate depends also on coatings defects (porosity, crystal defects, voids, etc.) so the higher defects density of coating systems obtained under magnetic stirring is responsible for the low Z_{mod} = 10 mHz values. The sonoelectrodeposited composite coatings showed the increase in Z_{mod} = 10 mHz value after 24 h in corrosion media, and this was particularly pronounced when 20 W cm^{-2} of ultrasound power was applied (for both ceria sources used). The Z_{mod} = 10 mHz values of Zn–Co–CeO_2 (CeO_2 sol, 20 W cm^{-2}) increased up to 96 h of immersion in NaCl solution to ~ 2000 Ω cm^2, being four times higher than for coatings deposited with magnetic stirring for both ceria source (plateau of below 400 Ω cm^2), and

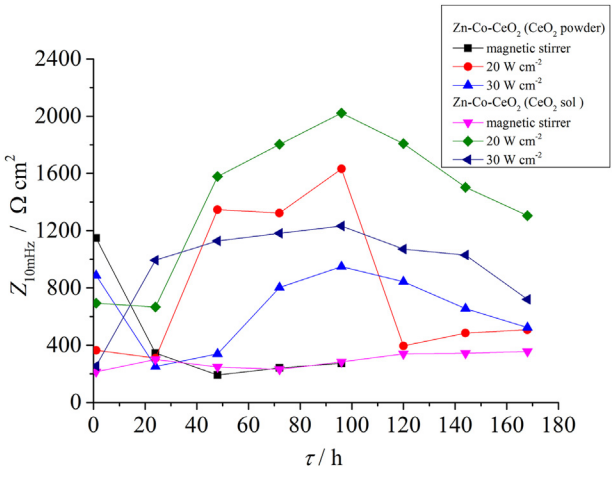

Fig. 11 – The impedance modulus values at low frequency (0.01 Hz) vs. immersion time in 3 wt% NaCl.

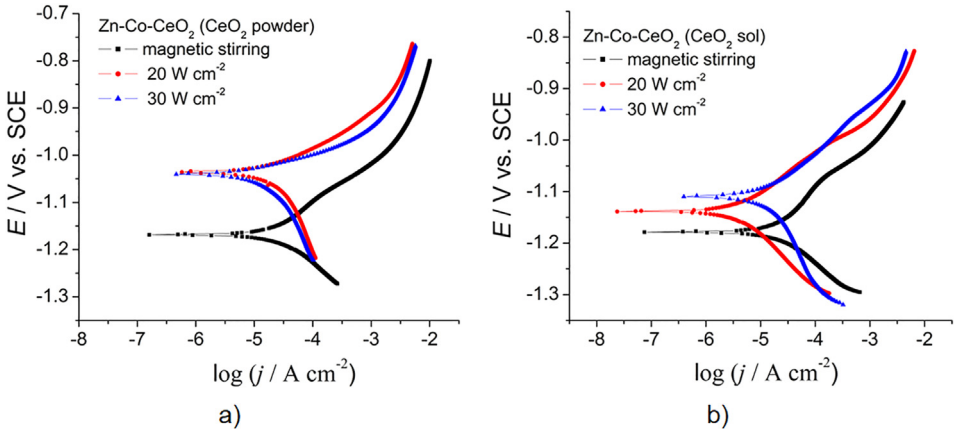

Fig. 12 – Polarization curves of: a) Zn–Co–CeO_2 (CeO_2 powder) and b) Zn–Co–CeO_2 (CeO_2 sol) for different agitation modes.

then gradually decreased during further immersion time. However, the $Z_{mod} = 10$ mHz values were still higher compared to other samples, suggesting the improved corrosion resistance of this coating. It showed the most uniform and dense structure (Fig. 6e,f), with the higher amount of incorporated ceria particles compared the Zn–Co–CeO_2 (CeO_2 powder) coatings. The high increase in protective ability of this system after the onset of corrosion processes (during first 24 h in NaCl solution) could be related to the self-healing effect provided by ceria particles [35,51]. Namely, it is possible that small ceria particles migrate and precipitate on the active corrosion sites, providing self-healing action. In our previous research [10] it was shown by the means of in situ AFM that this process is dynamic in nature, i.e. nanosized particles, that formed thin ceria layer on the metal substrate, detached and rearranged in real time while submerged in NaCl. Besides, reduction of CeO_2 to Ce_2O_3 occurs in corrosion media, so that Ce_2O_3 as soluble compound could release the Ce^{3+} ions into the solution [53] providing a self-healing action. The XPS analysis confirmed that a significant amount of Ce^{3+} was present in the synthesized ceria sol. Due to diffusion the Ce^{3+} ions reached the corroding area and formed thermodynamically favourable cerium-hydroxide ($Ce(OH)_4$) and oxide ($CeO_2 \cdot 2H_2O$) [53], slowing down the advancement of corrosion. This phenomena was not observed in Zn–Co alloy coatings [23], confirming the beneficial role of ceria in improving corrosion protection.

Table 4 – The values of corrosion potential, E_{corr}, and corrosion current density, j_{corr}, for Zn–Co–CeO_2 composite coatings.

Coating	Agitation mode	j_{corr} (μA cm^{-2})	$-E_{corr}$ (V)
Zn–Co–CeO_2 (CeO_2 powder)	Magnetic stirring	12.7	1.168
	20 W cm^{-2}	10.7	1.035
	30 W cm^{-2}	9.57	1.038
Zn–Co–CeO_2 (CeO_2 sol)	Magnetic stirring	8.40	1.179
	20 W cm^{-2}	3.15	1.136
	30 W cm^{-2}	7.40	1.110

Self-healing occurred in other composite samples as well, but the effect was less pronounced, since the corrosion resistance is actually interrelated between ceria content and coating morphology. So, the presence of ceria in composite coatings based on Zn–Co alloy offered two favourable actions in corrosion behaviour, increased barrier properties of composite coatings and self-healing effect, thereby providing a prolonged lifetime of Zn–Co alloy coatings.

Besides the electrochemical impedance spectroscopy tests, the polarization measurements were also performed. The Tafel polarization diagrams are presented at Fig. 12 and corrosion parameters calculated using Tafel extrapolation method (corrosion current density (j_{corr}) and corrosion potential (E_{corr}), are summarised in Table 4. The corrosion potential of Zn–Co–CeO_2 (CeO_2 powder) coating, produced under magnetic stirring, shifted from −1.168 V to more positive values when US was applied: −1.035 V and −1.038 V for 20 W cm^{-2} and 30 W cm^{-2}, respectively. The corrosion current density changed from 12.7 μA cm^{-2} (magnetic stirring) to 9.57 μA cm^{-2} (20 W cm^{-2} US power). Better protective properties of composite coatings obtained with utilizing sol were confirmed by their lower corrosion current densities. The lowest value of 3.15 μA cm^{-2} was determined for Zn–Co–CeO_2 (CeO_2 sol) composite coatings deposited under 20 W cm^{-2} US power. These results correlate well with the ones obtained EIS results, suggesting the increase in corrosion resistance for the composite coating where ceria sol is used as particles source and the deterioration of corrosion resistance with increase in ultrasound power.

4. Conclusions

Zn–Co–CeO_2 nanocomposite coatings were successfully electrodeposited on steel substrates. The source of ceria particles used in the plating solution along with type of agitation was shown to be crucial for the coatings performance. The synthesized ceria sol nanoparticles were more uniformly distributed in the plating solution and incorporated in the coating compared to ceria powder. The ultrasound (US)

agitation proved to be a better approach than magnetic stirring to provide powder de-agglomeration and suppress the formation of large particle aggregates in the plating solution (i.e. enabling homogeneous dispersion of particles). Nevertheless, the US agitation was not powerful enough to completely suppress the agglomeration phenomena in ceria powder, but when accompanied with utilizing ceria sol, better results could be achieved. The incorporation of ceria particles in Zn–Co matrix under magnetic stirring resulted in change of the deposit texture, i.e. from random oriented crystal to prismatic growth. Under ultrasound agitation the pyramidal preferential growth of deposit was favoured, which was beneficial for incorporating higher content of particles into the Zn–Co layer. The morphology of the composite coatings was improved by applied ultrasound power, especially 20 W cm^{-2} and coatings with the homogenous surface finish, without defects were produced. The use of the higher US power (30 W cm^{-2}) degraded the final coatings properties, i.e. compactness was deteriorated and, in turn, corrosion resistance. The most corrosion stable coating was shown to be Zn–Co–CeO_2 sol-derived coating, deposited under 20 W cm^{-2} ultrasound power.

Declaration of Competing Interest

The authors declare that they have no known competing financial interests or personal relationships that could have appeared to influence the work reported in this paper.

Acknowledgements

This research was financed by the Ministry for Scientific and Technological Development, Higher Education and Information Society of the Republic of Srpska (Contract No. 19.032/961-38/19) and the Ministry of Education, Science and Technological Development of the Republic of Serbia (Contract No. 451-03-9/2021-14/200135 and 451-03-9/2021-14/200017). This work was partially supported by the Ministerio de Ciencia e Innovación of the Spanish Government (project SURF-ERA, EXP-00137314/CER-20191003). The authors would like to acknowledge networking support by the COST Action MP1407.

REFERENCES

[1] Nemes PI, Zaharescu M, Muresan LM. Initial corrosion behavior of composite coatings obtained by co-deposition of zinc with nanoparticles of Ti and Ce oxides. J Solid State Electrochem 2013;17:511–8. https://doi.org/10.1007/s10008-012-1901-6.

[2] Xia X, Zhitomirsky I, McDermid JR. Electrodeposition of zinc and composite zinc-yttria stabilized zirconia coatings. J Mater Process Technol 2009;209(5):2632–40. https://doi.org/10.1016/j.jmatprotec.2008.06.031.

[3] Tuaweri TJ, Wilcox GD. Influence of SiO_2 particles on zinc-nickel electrodeposition. Trans IMF 2007;85(5):245–53. https://doi.org/10.1179/174591907X229608.

[4] Ranganatha S, Venkatesha TV, Vathsala K, Punith Kumar KM. Electrochemical studies on Zn/nano-CeO_2 electrodeposited composite coatings. Surf Coating Technol 2012;208:64–72. https://doi.org/10.1016/j.surfcoat.2012.08.004.

[5] Exbrayat L, Rebere C, Ndong Eyame R, Steyer P, Creues J. Corrosion behaviour in saline solution of pulsed-electrodeposited zinc-nickel-ceria nanocomposite coatings. Mater Corros 2017;68:1129–42. https://doi.org/10.1002/maco.201709419.

[6] Shourgeshty M, Aliofkhazraei M, Karimzadeh A. Study on functionally graded Zn-Ni-Al_2O_3 coatings fabricated by pulse-electrodeposition. Surf Eng 2018;35(2):1–9. https://doi.org/10.1080/02670844.2018.1432172.

[7] Camargo MK, Tudela I, Schmidt U, Cobley AJ, Bund A. Ultrasound assisted electrodeposition of Zn and Zn-TiO_2 coatings. Electrochim Acta 2016;198:287–95. https://doi.org/10.1016/j.electacta.2016.03.078.

[8] Vathsala K, Venkatesha TV. Zn-ZrO_2 nanocomposite coatings: electrodeposition and evaluation of corrosion resistance. Appl Surf Sci 2011;257(21):8929–36. https://doi.org/10.1016/j.apsusc.2011.05.067.

[9] Ghaziof S, Gao W. Zn-Ni-Al_2O_3 nanocomposite coatings prepared by sol-enhanced electroplating. Appl Surf Sci 2015;351:869–79. https://doi.org/10.1016/j.apsusc.2015.06.010.

[10] Stevanović S, Lekka M, Lanzutti A, Tesić N, ŽivkovićLj, Fedrizzi L, et al. Real-time AFM and impedance corrosion monitoring of environmentally friendly ceria films on AA7075. J Electrochem Soc 2020;167(10):101503. https://doi.org/10.1149/1945-7111/ab98af.

[11] Calvache-Muñoz J, Prado FA, Rodríguez-Páez JE. Cerium oxide nanoparticles: synthesis, characterization and tentative mechanism of particle formation. Colloid Surface Physicochem Eng Aspect 2017;529:146–59. https://doi:10.1016/j.colsurfa.2017.05.059.

[12] Kosacki I, Suzuki T, Anderson HU, Colomban P. Raman scattering and lattice defect in nanocrystaline CeO_2 thin films. Solid State Ionics 2002;149:99–105. https://doi.org/10.1016/S0167-2738(02)00104-2.

[13] Wu L, Wiesmann HJ, Moodenbaugh AR, Klie RF, Zhu Y, Welch DO, et al. Oxidation state and lattice expansion of CeO_{2-x} nanoparticles as a function of particle size. Phys Rev B 2004;69(12):125415. https://doi:10.1103/physrevb.69.12541.

[14] Karimzadeh A, Aliofkhazraei M, Walsh FC. A review of electrodeposited Ni-Co alloy and composite coatings: microstructure, properties and applications. Surf Coating Technol 2019;372:463–98. https://doi.org/10.1016/j.surfcoat.2019.04.079.

[15] Sadoun AM, Mohammed MM, Elsayed EM, Meselhy AF, El-KadyOA. Effect of nano Al_2O_3 coated Ag addition on the corrosion resistance and electrochemical behavior of Cu-Al_2O_3 nanocomposites. J Mater Res Technol 2020;9(3):4485–93. https://doi.org/10.1016/j.jmrt.2020.02.076.

[16] García-Lecina E, García -Urrutia I, Díez A, Fornell J, Pellicer E, Sort J. Codeposition of inorganic fullerene-like WS_2 nanoparticles in an electrodeposited nickel matrix under the influence of ultrasonic agitation. Electrochim Acta 2013;114:859–67. https://doi.org/10.1016/j.electacta.2013.04.088.

[17] Zhang D, NastacL. Numericalmodeling of the dispersion of ceramic nanoparticles during ultrasonic processing of aluminum-based nanocomposites. J Mater Res Technol 2014;3(4):296–302. https://doi.org/10.1016/j.jmrt.2014.09.001.

[18] Tudela I, Yhang Y, Pal M, Kerr I, Cobley AJ. Ultrasound-assisted electrodeposition of composite coatings with

particles. Surf CoatTechnol 2014;259(C):363–73. https://doi.org/10.1016/j.surfcoat.2014.06.023.
[19] Hyde ME, Compton RG. How ultrasound influences the electrodeposition of metals. J Electroanal Chem 2002;531(1):19–24. https://doi.org/10.1016/S0022-0728(02)01016-1.
[20] Tulio PC, Carlos IA. Effect of SiC and Al_2O_3 particles on the electrodeposition of Zn, Co, and Zn-Co: II. Electrodeposition in the presence of SiC and Al_2O_3 and production of ZnCo-SiC and ZnCo-Al_2O_3 coatings. J Appl Electrochem 2009;39:1305–11. https://doi.org/10.1007/s10800-009-9803-8.
[21] Arora S, Sharma B, Srivastava Ch. ZnCo-carbon nanotube composite coating with enhanced corrosion resistance behaviour. Surf Coating Technol 2020;398:126083. https://doi.org/10.1016/j.surfcoat.2020.126083.
[22] Bajat JB, Stankovic S, Jokic BM. Electrochemical deposition and corrosion stability of Zn-Co alloy. J Solid State Electrochem 2009;13:755–62. https://doi.org/10.1007/s10008-008-0604-5.
[23] Riđošić M, García-Lecina E, Salicio-Paz A, Bajat J. The advantage of ultrasound deposition on morphology and corrosion stability of Zn-Co alloy coatings. Trans IMF 2020;98(3):1–7. https://doi.org/10.1080/00202967.2020.1748390.
[24] Li B, Zhang W. Syntesis of Ni-Co-ZrO_2 nanocomposite doped with ceria particles via electrodeposition as high protective coating. J Alloys Compd 2020;820:153158. https://doi.org/10.1016/j.jallcom.2019.153158.
[25] Phoka S, Laokul P, Swatsitang E, Promarak V, Seraphin S, Maensiri S. Synthesis, structural and optical properties of CeO_2 nanoparticles synthesized by a simple polyvinyl pyrrolidone (PVP) solution route. Mater Chem Phys 2009;115(1):423–8. https://doi.org/10.1016/j.matchemphys.2008.12.031.
[26] Zawadzki M. Preparation and characterization of ceria nanoparticles by microwave-assisted solvothermal process. J Alloys Compd 2008;454(1–2):347–51. https://doi.org/10.1016/j.jallcom.2006.12.078.
[27] Hu C, Zhang Z, Liu H, Gao P, Lin Wang Z. Direct synthesis and structure characterization of ultrafine CeO_2 nanoparticles. Nanotechnology 2006;17(24):5983–7. https://doi.org/10.1088/0957-4484/17/24/013.
[28] Meng F, Wanga L, Cui J. Controllable synthesis and optical properties of nano-CeO_2 via a facile hydrothermal route. J Alloys Compd 2013;556:102–8. https://doi.org/10.1016/j.jallcom.2012.12.096.
[29] Srivastava M, Kumar Das A, Khanra P, Elias Uddin Md, Hoon Kim N, Hee Lee J. Characterizations of in situ grown ceria nanoparticles on reduced graphene oxide as a catalyst for the electrooxidation of hydrazine. J Mater Chem 2013;1:9792–801. https://doi.org/10.1039/C3TA11311F.
[30] Pfau A, Schierbaum KD. The electronic structure of stoichiometric and reduced CeO_2 surface: an XPS, UPS, and HREELS study. Surf Sci 1994;321(1–2):71–80. https://doi.org/10.1016/0039-6028(94)90027-2.
[31] Wang L, Meng F. Oxygen vacancy and Ce^{3+} ion dependent magnetism of monocrystal CeO_2nanopoles synthesized by a facile hydrothermal method. Mater Res Bull 2013;48(9):3492–8. https://doi.org/10.1016/j.materresbull.2013.05.036.
[32] Ferreira NS, Angelica RS, Marques VB, Lima CCO, Silva MS. Cassava-starch-assisted sol–gel synthesis of CeO_2 nanoparticles. Mater Lett 2016;165:139–42. https://doi.org/10.1016/j.matlet.2015.11.107.
[33] Chen H, Jiang Z, Li X, Lei X. Effect of cerium nitrate concentration on morphology, structure and photocatalytic activities of CeO_2 nanoparticles synthesized by microwave interface method. Mater Lett 2019;257:126666. https://doi.org/10.1016/j.matlet.2019.126666. 257.
[34] Holgado JP, Alvarez R, Munuera G. Study of CeO_2 XPS spectra by factor analysis: reduction of CeO_2. Appl Surf Sci 2000;161(3–4):301–15. https://doi.org/10.1016/S0169-4332(99)00577-2.
[35] Montemor MF, Pinto R, Ferreira MGS. Chemical composition and corrosion protection of saline films modified with CeO_2 nanoparticles. Electrochim Acta 2009;54(22):5179–89. https://doi.org/10.1016/j.electacta.2009.01.053.
[36] Aramaki K. A Self-healing protective film prepared on zinc by treatment in a Ce(NO3)3 solution and modification with Ce(NO3)3. Corrosion Sci 2005;47(5):1285–98. https://doi.org/10.1016/j.corsci.2004.05.022.
[37] Yoganandan G, PradeepPremkumar K, Balaraju JN. Evaluation of corrosion resistance and self-healing behavior of zirconium–cerium conversion coating developed on AA2024 alloy. Surf Coating Technol 2015;270:249–58. https://doi.org/10.1016/j.surfcoat.2015.02.049.
[38] Li B, Zhang W, Mei T, Du S, Li D, Miao Y. Influence of zirconia and ceria nanoparticles on structure and properties of electrodeposited Ni-W nanocomposite. Comp Struct 2020;235:111773. https://doi.org/10.1016/j.compstruct.2019.111773.
[39] Ma CY, Zhao DQ, Xia FF, Xia H, Williams T, Xing HY. Ultrasonic-assisted electrodeposition of Ni-Al_2O_3 nanocomposite at various ultrasonic powers. Ceram Int 2020;45(5):6115–23. https://doi.org/10.1016/j.ceramint.2019.11.075.
[40] Brenner A. Electrodeposition of alloys, vols. 1 and 2. New York: Academic Press; 1963.
[41] Mounaga M, Ricq L, Bercot P. Electrodeposition and Characterization of zinc-cobalt alloy from chloride bath; influence of coumarin as additive. Surf Coating Technol 2008;202(9):1645–51. https://doi.org/10.1016/j.surfcoat.2007.07.023.
[42] Gharahcheshmeh MH, Sohi MH. Study of corrosion behaviour of zinc and Zn-Co alloy electrodeposits obtained from alkaline bath using direct current. Mater Chem Phys 2009;117(2–3):414–21. https://doi.org/10.1016/j.matchemphys.2009.06.009.
[43] Bajat JB, Stankovic S, Jokic BM. Electrochemical deposition and corrosion stability of Zn-Co alloys. J Solid State Electrochem 2009;13:755–62. https://doi.org/10.1007/s10008-008-0604-5.
[44] Alfantazi AM, Gharahcheshmeh MH, Sohi MH. Electrochemical studies of zinc-cobalt alloy coatings deposited from alkaline baths containing glycine as complexing agent. J Appl Electrochem 2010;40:1563–70. https://doi.org/10.1007/s10800-010-0142-6.
[45] Li Y, Wang G, Liu S, Zhao S, Zhang K. The preparation of Ni/GO composite foils and the enhancement effects of GO in mechanical properties. Comp Part B 2018;135:43–8. https://doi.org/10.1016/j.compositesb.2017.09.064.
[46] Wang C, Shen L, Qiu M, Tian Z, Jiang W. Characterizations of Ni-CeO_2 nanocomposite coating by interlaced jet electrodeposition. J Alloys Compd 2017;727:269–77. https://doi:10.1016/j.jallcom.2017.08.105.
[47] Sheng M, Weng W, Wang Y, Wu Q, Hou S. Co-W/CeO2 composite coatings for highly active electrocatalysis of hydrogen evolution reaction. J Alloys Compd 2018;743:682–90. https://doi: 10.1016/j.jallcom.2018.01.356.
[48] Berube LPH, L'Esperance G. A quantitative method of determining the degree of texture of zinc electrodeposits. J Electrochem Soc 1989;136(8):2314–5. https://doi.org/10.1149/1.2097318.
[49] Li B, Zhang W. A novel Ni-B/YSZ nanocomposite coating prepared by a simple one-step electrodeposition at different

duty cycles. J Mater Res Technol 2020;9(2):1519–29. https://doi.org/10.1016/j.jmrt.2019.11.077.

[50] Calado LM, Taryba MG, Carmezim MJ, Montemor MF. Self-healing ceria-modified coating for corrosion protection of AZ31 magnesium alloy. CorrSci 2018;142:12–21. https://doi.org/10.1016/j.corsci.2018.06.013.

[51] Ma Y, Yhang Y, Liu J, Ge Y, Yan X, Sun Y, et al. GO-modified double-walled polyurea microcapsules/epoxy composites for marine anticorrosive self-healing coating. Mater Des 2020;189:108547. https://doi.org/10.1016/j.matdes.2020.108547.

[52] Cambon JB, Ansart F, Bonino JP, Turq V. Effect of cerium concentration on corrosion resistance and polymerization of hybrid sol-gel coating on martensitic stainless steel. Prog Org Coating 2012;75(4):486–93. https://doi.org/10.1016/j.porgcoat.2012.06.005.

[53] Guergova D, Stoyanova E, Stoychev D, Avramova I, Stefanov P. Self-healing effect of ceria electrodeposited thin films on stainless steel in aggressive 0.5 mol/L NaCl aqueous solution. J Rare Earths 2015;33(11):1212–27. https://doi.org/10.1016/S1002-0721(14)60548-2.